Prof. Cagri Savran's research group at Purdue University focuses on development of novel micro and nano systems for detection of diagnostic biomarkers with a special emphasis on high throughput and point-of-care technologies.

Title: Circulating tumor cell detection using a parallel flow micro-aperture chip system

Circulating tumor cells (CTCs) in blood are detected using a high flow-rate micro-aperture chip system. The sample mixture that contains CTCs tagged with magnetic particles runs parallel to the microchip for on-chip isolation and enumeration of CTCs.

As featured in:

Lab on a Chip

ROYAL SOCIETY OF CHEMISTRY

www.rsc.org/loc

Lab on a Chip
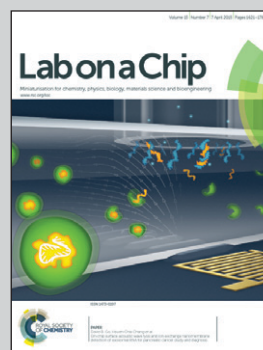
CrossMark
click for updates

Circulating tumor cell detection using a parallel flow micro-aperture chip system†

Chun-Li Chang,[ab] Wanfeng Huang,[ab] Shadia I. Jalal,[d] Bin-Da Chan,[ab] Aamer Mahmood,[b] Safi Shahda,[d] Bert H. O'Neil,[d] Daniela E. Matei[d] and Cagri A. Savran*[abc]

We report on-chip isolation and detection of circulating tumor cells (CTCs) from blood samples using a system that integrates a microchip with immunomagnetics, high-throughput fluidics and size-based filtration. CTCs in a sample are targeted *via* their surface antigens using magnetic beads functionalized with antibodies. The mixture is then run through a fluidic chamber that contains a micro-fabricated chip with arrays of 8 μm diameter apertures. The fluid runs parallel to the microchip while a magnetic field is generated underneath to draw the beads and cells bound to them toward the chip surface for detection of CTCs that are larger than the apertures and clear out free beads and other smaller particles bound to them. The parallel flow configuration allows high volumetric flow rates, which reduces nonspecific binding to the chip surface and enables multiple circulations of the sample fluid through the system in a short period of time. In this study we first present models of the magnetic and fluidic forces in the system using a finite element method. We then verify the simulation results experimentally to determine an optimal flow rate. Next, we characterize the system by detecting cancer cell lines spiked into healthy human blood and show that on average 89% of the spiked MCF-7 breast cancer cells were detected. We finally demonstrate detection of CTCs in 49 out of 50 blood samples obtained from non-small cell lung cancer (NSCLC) patients and pancreatic cancer (PANC) patients. The number of CTCs detected ranges from 2 to 122 per 8 mL s of blood. We also demonstrate a statistically significant difference between the CTC counts of NSCLC patients who have received therapy and those who have not.

Introduction

Circulating tumor cells (CTCs) are rare cells present in the blood of cancer patients. They are shed from both primary and metastatic tumors and are believed to play a key role in cancer progression.[1–5] CTCs can serve as indicators of metastatic disease and possibly recurrence after surgery in some tumor types. The CTC count has been reported to correlate with overall tumor burden, and hence CTCs have been proposed as a tool for monitoring disease progression and response to therapy.[6–9] Another major advantage of CTCs is that they can be further interrogated after detection. For example, sequencing of the genome and transcriptome could

reveal mutations or quantitate gene expression. The detected cells also have the potential to be cultured, grown and tested with different combinations of chemotherapeutic agents for drug discovery and personalized medicine. Finally, increasing amounts of data suggest that cancer is a very heterogeneous disease.[10] Different parts of the same tumor sample have shown heterogeneity in drug target expression in addition to the differences that have been identified between primary tumors and their metastatic counterparts.[11] Since metastasis represents the major cause of cancer death,[1,12] understanding the biology of this complicated process is extremely important, and could be facilitated by CTC analysis.

Detecting CTCs however is a challenging task because of their scarcity in blood samples (as few as 1 or less per mL). Hence, a reliable analysis requires large volumes (several mL s) of samples.[8,9,13] Currently one of the most widely used standard systems to detect cells is flow cytometry, which can separate and recover cells at high yield and purity. However, its volumetric throughput is generally low due to cells passing in single file, and its operational costs can be high. These factors make it challenging to detect extremely rare CTCs using flow cytometry.[14]

a School of Mechanical Engineering, Purdue University, West Lafayette, IN, 47907, USA. E-mail: savran@purdue.edu
b Birck Nanotechnology Center, Purdue University, West Lafayette, IN, 47907, USA
c Weldon School of Biomedical Engineering, Purdue University, West Lafayette, IN, 47907, USA
d Department of Medicine, Indiana University School of Medicine, Indianapolis, IN, 46202, USA
† Electronic supplementary information (ESI) available. See DOI: 10.1039/c5lc00100e

Numerous systems have been developed for CTCs detection. Among all, the CellSearch System is currently the only FDA-cleared platform for CTC test for metastatic breast, prostate and colorectal cancers.[15,16] This system uses magnetic beads conjugated with antibodies against epithelial cell adhesion molecule (EpCAM) to immunomagnetically separate CTCs from blood samples that are previously fixed in tubes at the moment of sample collection. The isolated cells are then subjected to immunofluorescence using 4,6-diamidino-2-phenylindole (DAPI, for DNA in cell nuclei) and antibodies against cytokeratin (for epithelial cell) and CD45 (for white blood cells) for CTC identification. One of the limitations of the CellSearch system is its low detection efficiency due to targeting of only one surface marker (EpCAM), leading to CTCs being identified in as low as 65% of patients known to have metastatic diseases.[15] Also the blood samples are immediately fixed in the collection tube prior to detection and hence the captured cells are not viable after isolation, limiting the options for post-isolation analyses.[17–20]

In recent years, researchers have developed a number of microfluidic-based, lab-on-a-chip devices that can perform precise and highly sensitive detection of rare cells. For example, the Toner and Haber Groups developed the ground breaking 'CTC-chip' device in 2007 that isolates CTCs by flowing blood samples through a chip composed of an array of antibody-functionalized micro-posts to capture CTCs.[8] In 2010 they developed a 'herringbone-chip' on which the micro-pattern was designed for optimal fluidic mixing to capture target CTCs.[9] Recently the same groups developed the microfluidic "CTC-iChip" system that integrates hydrodynamic cell sorting, inertial focusing, and magnetophoretic separation of white blood cells and CTCs.[21,22] Sheng *et al.* captured CTCs using microfluidic devices in which the micro-structures were functionalized with high-affinity aptamers or gold nanoparticles conjugated with aptamers instead of antibodies.[23,24] Hoshino *et al.* built a microfluidic channel by bonding a patterned PDMS interface on a smooth glass slide placed on top of an array of 3 magnets. CTCs captured by magnetic nanoparticles in the sample fluid were attracted to the glass slide in a flow and were dried for downstream fluorescent analysis.[25] Earhart and co-workers labeled tumor cells in blood samples with magnetic nanoparticles conjugated with anti-EpCAM antibodies and passed the sample through the channels of a micro-fabricated sifter in the present of a magnetic field. The cell–particle complexes were then magnetically attracted to the channel walls as they passed through.[26] It is also possible to use magnetic particles to perform isolation of CTCs using commercially available MACS (Magnetic Activated Cell Sorting) columns, although generally these columns are used in conjunction with an additional instrument to perform detection such as flow cytometers.

Researchers have also developed CTC detection systems that do not rely on affinity. This type of isolation relies on discriminating cells based on their size, and hence can usually perform label free cell sorting. An intuitive way to achieve this is by forcing the blood sample through a filter that contains a porous membrane or micro-structures to physically stop and retain larger cells like CTCs and allow passage of smaller blood cells.[27–32] Another approach to discriminate cells based on their shapes and dimensions is by engineering micro-channels and sample flow rates to employ size-dependent hydrodynamic forces on cells flowing in the channel so that larger tumor cells are separated from smaller blood cells.[20,33]

We have developed a system that integrates a microchip with parallel fluidic flow to perform high throughput immunomagnetic as well as size-based separation for detection of rare cells. This particular integration enables all of the following advantages that are normally difficult to co-exist in a single platform: 1) immunomagnetics using a cocktail of antibodies allows affinity-based specific capture of CTCs, 2a) high flow rate allows a simple way to wash away unwanted cells and improve the detection purity, 2b) as well as rapid re-circulation of the sample within the fluid system, and 3) the microchip with an array of micro-apertures operated with a dual magnet configuration captures larger CTCs and filters out smaller magnetic particles further improving purity (see Fig. S1 in the ESI†) and allowing versatility to either wash out the captured cells for collection or analyze them on the chip surface. We have reported a preliminary study with an earlier version of the system to demonstrate its capability to detect cell lines.[34,35] We herein demonstrate the detection of actual CTCs from blood samples of cancer patients, as well as the system's modeling and characterization.

The detection strategy is illustrated in Fig. 1(a). Antibody-conjugated magnetic beads (1 μm) are first incubated with the sample that contains CTCs whose size usually ranges from 10 to 30 μm. The sample mixture then flows parallel to a micro-aperture chip at a relatively high flow rate (mL s min^{-1}, as opposed to μL s min^{-1} achieved in most microfluidic cell detection systems) while a magnetic field is introduced at the bottom of the chamber to apply a vertical attractive force on the magnetic beads. The targeted cells bound with magnetic particles, as well as free magnetic particles are attracted to the chip surface while the majority of other entities are washed away under the effect of high flow rate (shown in Fig. 1(b)). The magnetized entities that are larger than the apertures (8 μm), such as CTCs bound with beads, are held on the chip surface while smaller magnetic entities such as unbound free beads and some blood cells bound with beads are filtered out. Often, an undesired effect occurs where many free magnetic beads still remain on the chip surface if they do not initially find an aperture to pass through. To alleviate this problem, a secondary, smaller magnet is situated on the top of the fluidic chamber in a stable orientation where it is attracted by the larger magnet in the bottom. The second magnet is subjected to an oscillating horizontal motion (Fig. 1(c)) which perturbs the horizontal magnetic force applied on the beads and therefore guides them to adjacent apertures. The captured cells are then analyzed using immunofluorescence while they are still on the chip surface for identification and enumeration (Fig. 1(d)).
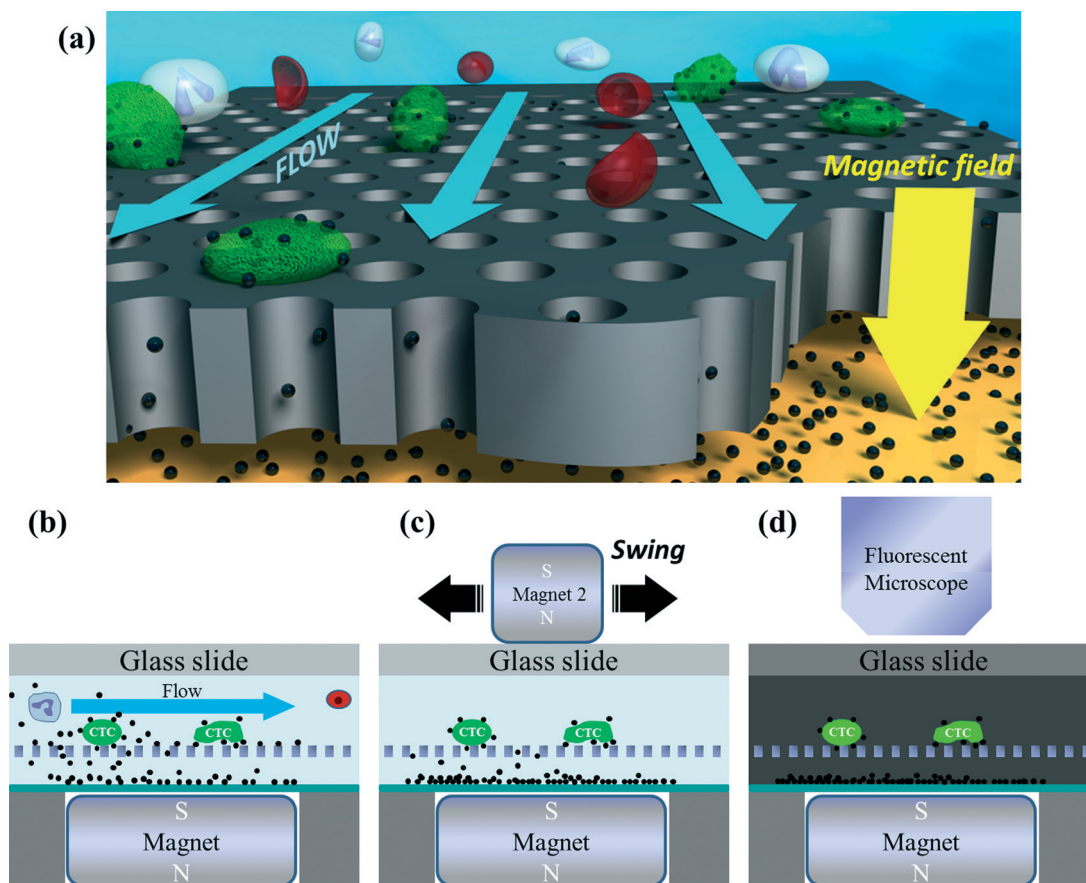
Fig. 1 (a) Schematic of the detection strategy of the micro-aperture chip system for CTC detection, and cross-section views of the fluidic chamber illustrating (b) capturing of CTCs and beads in a flow, (c) maneuvering of a second magnet on top of the chamber to guide the free beads on the chip surface down through the apertures, and (d) the on-chip fluorescent microscopy for CTC identification and enumeration.

The system is relatively simple, versatile and compatible with existing laboratory practices. The user can analyse the captured cells directly on-chip (as we demonstrated in this study), and/or release them for storage or further analysis which also allows re-using the chip. The system has a high volumetric throughput with flow rates of milliliters min^{-1}, which allows circulating the sample fluid through the fluidic system multiple times quickly, and reduces nonspecific binding of most blood cells on the chip surface. Here, we first demonstrate a model that uses finite element analysis to help understand the physical operation of the system as well as to find the parameters for optimal system performance. We verify the simulation by spiking 70 MCF-7 cells pre-labeled with magnetic beads that are conjugated with antibodies against EpCAM (anti-EpCAM) into blood and study the relationship between the capture yield and flow rate. We then characterize the yield of the system by detecting unlabeled MCF-7 cells spiked into blood (from 0 to 110 cells/8 mL) to mimic analysis of blood samples obtained from cancer patients. We finally demonstrate the utility of the system in detecting CTCs in blood samples collected from patients with non-small cell lung cancer (NSCLC, $N = 38$) and pancreatic cancer (PANC, $N = 12$).

In the current system the choice of antibodies is not limited to anti-EpCAM. It is possible to combine groups of beads wherein each group is conjugated with antibodies to target a different CTC surface antigen. For example, studies show that higher rates of epidermal growth factor receptor (EGFR) overexpression were found in NSCLC patients in later stage (around 50% in stage III).[36] It has also been shown that over 90% of the pancreatic cancer cells overexpress the carcinoembryonic antigen (CEA).[37] Hence, in addition to anti-EpCAM beads, we also used anti-EGFR beads in NSCLC samples and anti-CEA in PANC samples. Recently, additional studies have been showing that tumor cells could undergo epithelial-to-mesenchymal transition (EMT) which could result in downregulation of epithelial markers and upregulation of mesenchymal markers such as vimentin.[38–43] In order to also capture such CTCs, magnetic beads conjugated with antibodies against vimentin (anti-VMT) were also used while analysing NSCLC samples.

Materials and methods

Chip fabrication and experimental setup

The microchips that contain an array of 8 μm apertures in the center were produced using conventional silicon

fabrication processes. The fabrication was performed on double-side-polished, <100> oriented intrinsic silicon wafers with a thickness of 550 μm, and the process flow was described in a previous study.[34] At the end of the fabrication process, 8 microchips (40 mm by 20 mm), each with a 9 mm by 3 mm porous area (50 μm thick) at the center, were obtained from a single 4" silicon wafer. Fig. 2(a) shows a SEM image of the porous area of a microchip.

To configure the experimental setup, a fluidic chamber was first constructed by placing a layer of polydimethylsiloxane (PDMS, ~2 mm-thick) on a microchip as a spacer and covered with a 1 mm-thick glass slide. The inlet and outlet of the fluidic chamber were opened on the cover slide. The dimension of the fluidic channel that encloses the porous area was defined by patterning the PDMS using a laser cutter (Universal Laser Systems, VLS 3.60) to have a 30 mm by 3.8 mm grove. The bottom of the microchip was also sealed with a thin layer of PDMS coated on a transparency film (3M PP2500). The thickness of the PDMS-transparency film complex was 0.1 mm. The assembled fluidic chamber was mounted on a hollow acrylic stand (shown in Fig. 2(b)), in which a neodymium permanent magnet (K&J Magnetics, grade N52) could be inserted to provide a magnetic field. The inlet of the chamber was connected to the fluidic sources while the outlet was connected to a peristaltic pump (Ismatec

ISM596B) and drained into a waste container or a collection tube (Fig. 2(c)).

System modeling and simulation

To understand the underlying forces in the system and to determine optimal parameters for system operation, a finite element model was built using the modeling software COMSOL Multiphysics 4.3a (COMSOL, Inc.). We first built the models of both magnetic and fluidic fields based on the magnets used and the geometric parameters of the fluidic chamber. The magnetic force, the fluidic drag force, as well as gravity were considered to act simultaneously on free beads or cells that are bound to multiple beads. The trajectories of the objects entering the chamber were then calculated by using the particle tracing module in COMSOL. Based on the simulation results we also calculated an estimated percentage of the number of particles reaching the chip surface.

We also investigated the lateral movement of the free beads on the microchip's surface resulting from the motion of an additional magnet situated on the top of the fluidic chamber. In this case we modeled the magnetic fields in the chamber that result from the two-magnet configuration. While modeling this particular effect, the fluidic flow field was ignored since during an experiment this step is
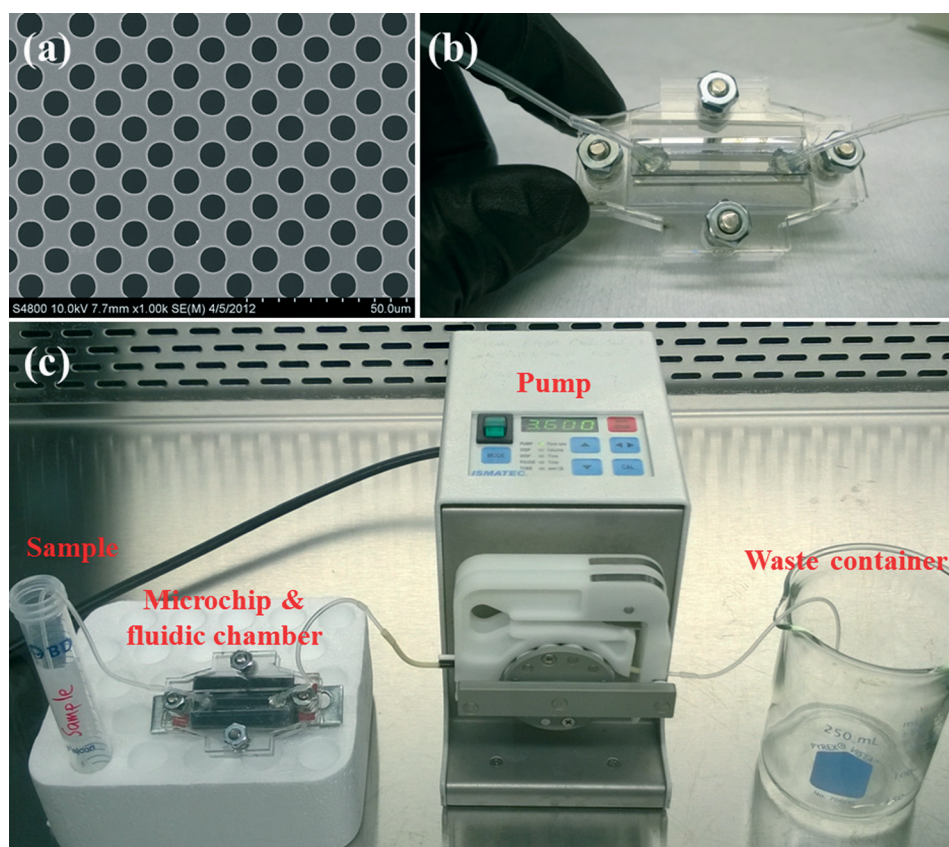

Fig. 2 (a) A SEM image of a fabricated micro-aperture chip. (b) A picture of the microfluidic chamber assembly and (c) the experimental setup.

performed after the target entities have been captured on the chip surface and the flow has stopped.

Detecting MCF-7 cells spiked into blood

We performed an initial characterization of the system by detecting known number of cells spiked into healthy human blood. A series of suspensions were prepared by spiking 0 to 110 MCF-7 (breast cancer cell line) cells into 8 mL of blood collected from healthy donors under an approved IRB protocol. The spiked blood samples were first treated with a red blood cell (RBC) lysis buffer (G-Biosciences) followed by centrifugation to remove the supernatant. The remaining cells were re-suspended in 1.5 mL of phosphate buffered saline (PBS, Invitrogen) and incubated with 4 μL (40 μg) of anti-EpCAM beads at 4 °C for 1 hour. The sample was then circulated in the fluidic chamber (with the bottom magnet in place) at a flow rate of 2 mL min^{-1} for 3 minutes, which was followed by washing with 3 mL of PBS solution. The captured cells were fixed on the chip and subjected to immunofluorescence analysis to identify and enumerate the MCF-7 cells.

CTC detection in blood samples of NSCLC and PANC patients

Patients with advanced NSCLC and PANC were recruited for this study under an approved IRB protocol. Blood samples from 38 NSCLC and 12 PANC were collected. An 8 mL blood sample from each patient was either divided into 2 equal volumes of 4 mL s or used as a single 8 mL entity for examination. A combination of anti-EpCAM, anti-EGFR and anti-VMT beads (1 : 1 : 1) were used with the NSCLC samples; and a combination of anti-EpCAM and anti-CEA beads (1 : 1) were used with the PANC samples. A group of beads was functionalized with only one type of an antibody. Multiple bead groups, each containing a different antibody were then added into the sample mixtures for incubation. The rest of the protocol was the same as that used in the detection of MCF-7 cells spiked into blood.

Blood sample collection and preparation

Blood donated by healthy volunteers as well as NSCLC and PANC patients was collected in BD Vacutainer tubes with additives of either acid citrate dextrose (ACD) solution A or sodium polyanethol sulfonate (SPS). Blood samples were kept at 4 °C starting immediately after collection until the detection process which occurred within 12 hours of collection.

Preparation of magnetic beads conjugated with antibodies

Antibodies against EpCAM, EGFR, CEA and VMT were separately conjugated to magnetic beads freshly before detection. Biotinylated polyclonal antibodies against human EpCAM and CEA were purchased from R&D systems. Biotinylated monoclonal antibodies against human EGFR and VMT were purchased from Abcam. Streptavidin conjugated superparamagnetic beads with 1 μm diameter were obtained from

Sigma Aldrich. We saturated the beads (20 μL, 10 mg mL^{-1}) with excess amounts of antibodies (10 μL, 0.2 mg mL^{-1}) in PBS at room temperature for 1 hour, followed by rinsing with PBS three times on a magnetic stand and re-suspending in PBS.

Cell culturing and preparation of cell suspensions

The breast cancer cell line MCF-7, obtained from American Type Culture Collection (ATCC), was cultured in Eagle's Minimum Essential Medium (EMEM, ATCC) with 0.01 mg ml^{-1} bovine insulin (Sigma-Aldrich) and 10% fetal bovine serum (FBS, Gemini Bio Products). Cultured cells were harvested using Trypsin-EDTA (Invitrogen), and were re-suspended and diluted in culture media immediately before cell detection experiments. The original cell concentrations were determined by placing 3 μL of the cell suspension on a glass slide to count the cells using a bright field microscope and calculating the average from 4 measurements. The cell suspension was then spiked into blood to achieve the desired concentrations.

Immunofluorescence analysis

Cells captured on the microchip surface were first fixed using a 4% paraformaldehyde (PFA) solution in PBS and then labeled fluorescently while the microchip was in the fluidic chamber. Anti-pan Cytokeratin monoclonal antibodies conjugated with FITC (anti-CK-FITC, Abcam, USA), anti-CD45 monoclonal antibodies (to rule out white blood cells) conjugated with phycoerythrin (anti-CD45-PE, Abcam, USA), and DAPI to verify nucleated cells (Sigma-Aldrich, USA) were introduced into the chamber at the same time and incubated for 1 hour at room temperature to label the cells. After washing away the unbound antibody-dye with 3 mL of PBS, the microchip was inspected while still in the fluidic chamber using a fluorescent microscope (ECLIPSE 80i, Nikon) with a Fiber illuminator (C-HGFI, Nikon).

Results and discussion

(1) System modeling and simulation

Detection mode. We primarily studied the effects of flow rate on the trajectory of cells within the fluidic chamber when they are bound by various numbers of magnetic beads. We simulated a scenario where 100 cells, each bound with a given number of beads, flow though the fluidic chamber under the influence of a high volumetric flow rate that varies from 1 to 5 mL min^{-1}. The dimensions of the fluidic chamber used in the simulation were ($L \times W \times D = 30 \times 3.8 \times 2$ mm), which are defined by a PDMS spacer in the fluidic chamber. The experimental parameters yield a Reynold's number of 4.58 indicating that the flow in the chamber is in general laminar. To simplify our simulation we assumed that the porous structure does not have any significant effects on the bulk fluidic field. We also assumed that the mutual magnetization among the beads, as well as the coupling between the

fluidic and magnetic fields were negligible. The forces acting on a cell–beads complex in the chamber included the magnetic force, the drag force induced by the flow, gravity, and the buoyant force. We further assumed that the magnitude of the magnetic force acting on each cell–bead complex is proportional to the number of the beads bound to that particular cell, since this force acts directly on the beads, and not on the cells themselves. The magnetic force $\overrightarrow{F_m}$, which is one of the dominant forces in the system, can be expressed by:[25,44]

$$\overrightarrow{F_m} = N \frac{V_b \chi}{2\mu_0} \nabla \left(\vec{B} \cdot \vec{B} \right) \quad (1)$$

where N is the number of beads attached to a cell; V_b is the volume of a single bead (5.24×10^{-19} m³); χ the effective volumetric magnetic susceptibility (2.7 unitless); μ_0 the vacuum permeability; and $\vec{B}$ the magnetic flux density (produced by the N52 magnet), which is shown in Fig. 3(a). The resulting magnetic force applied on a single bead at the detection surface of the microchip is shown in Fig. 3(b), where the green dashed line represents the magnitude of the vertical force (negative indicates a downward force) while the blue solid line represents the magnitude of the longitudinal force (positive indicates a force to the right).
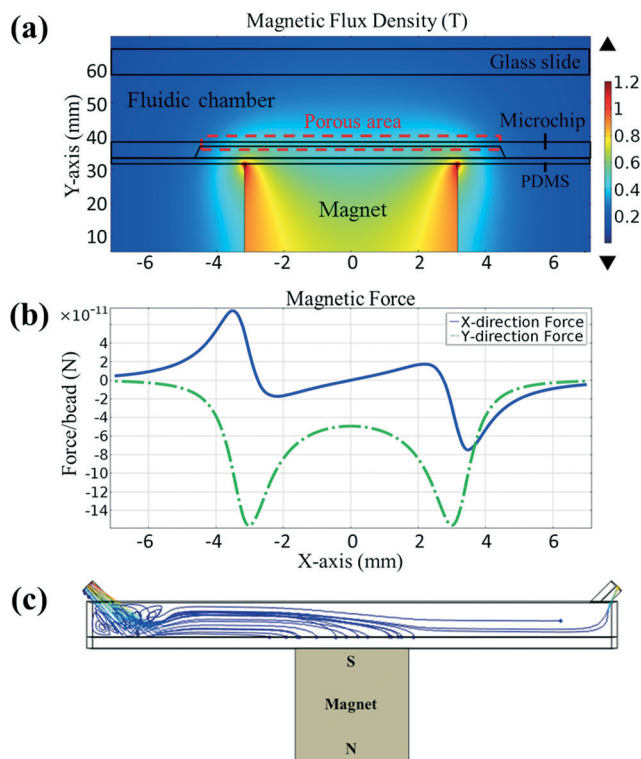

Fig. 3 (a) The simulated magnetic flux density pattern of a N52 magnet and (b) the corresponding magnetic force applied on a single bead in the fluidic chamber. The green dashed line shows the magnitude of the vertical force while the blue solid line indicates the magnitude of the horizontal force. (c) Illustration of simulated trajectories of cell–beads complexes in the fluidic chamber.

The fluid drag force $\overrightarrow{F_d}$, the other dominant force, acting on a cell–beads complex is given by:[45]

$$\overrightarrow{F_d} = 6\pi\eta r_p \left(\vec{U} - \overrightarrow{V_p} \right) \quad (2)$$

where η is the fluid dynamic viscosity (2.5×10^{-3} kg m⁻¹ × s for processed blood sample); r_p the radius of particle (5 μm for a MCF-7 cell); $\vec{U}$ the velocity of fluid; and $\overrightarrow{V_p}$ the velocity of particle.

The gravitational force applied on a complex is:

$$\overrightarrow{F_g} = m_p \vec{g} \quad (3)$$

where $\vec{g}$ is the gravitational acceleration and m_p is the mass of the cell–beads complex. The average mass of a dry MCF-7 cell, which is approximately 30% of the original mass, was measured to be 0.43 ng using a cantilever-based resonator.[46] The mass of a single magnetic bead with 1 μm diameter is around 1 pg. Hence the mass of a single cell bound with N beads is $1433 + N$ pg.

The buoyant force can be expressed by:

$$\overrightarrow{F_b} = -\vec{g}\rho V \quad (4)$$

where ρ is the density of the fluid (~1000 kg m⁻³) and V is the volume of a cell–beads complex, which is approximately 5.24×10^{-16} m³.

The contribution of gravitation (~14 pN) and buoyancy (~5 pN) are relatively small, yet their inclusion in the model is straightforward. Applying the Newton's second law yields:

$$m_p \frac{d\overrightarrow{V_p}}{dt} = \overrightarrow{F_m} + \overrightarrow{F_d} + \overrightarrow{F_g} + \overrightarrow{F_b} \quad (5)$$

We applied the particle tracing module in COMSOL to solve for the velocity and the displacement of the cell–beads complexes (as demonstrated in Fig. 3(c)). Based on the obtained trajectories the percentage of the cell–beads complexes reaching the microchip surface was estimated.

To accomplish this, we first experimentally determined N (eqn (1)), and used it in our computational model to study the effect of flow rate on the rate with which the cells encounter the surface of the chip.

In order to understand the extent of the specificity in the binding of beads, we studied how anti-EpCAM beads bind to MCF-7 cells as well as WBCs. Around 200 MCF-7 cells, as well as white blood cells (WBCs) isolated from 4 mL of healthy blood were first suspended in two separate tubes, added to 1.5 mL of PBS buffer, and incubated with 4 μL (40 μg) of anti-EpCAM beads at 4 °C for over 1 hour. The cells were aspirated using a micro-pipettor, transferred onto a glass slide and the beads on their surfaces were counted using a bright-field microscope with high magnification. The number of beads bound to each MCF-7 cells ranged from 3 to 63 with an average of 16.8 beads per cell, while majority of the WBCs

(>99%) did not bind to any bead at all. For those WBCs that did bind to beads, the number of beads found on each WBC ranged from 1 to 19 with a mean of 2.3 beads per cell. The distribution of number of beads on each cell group is shown in Fig. 4(a) (the relative frequency for WBCs was calculated only for those that bound with beads). The histograms of MCF-7 and WBCs overlapped mainly when $N < 10$. Fig. 4(a) also shows that around 90% of the MCF-7 bound to at least 7 beads, while around 90% of the bead-bound WBCs had 1 to 4 beads.

Using this information, we next simulated the trajectories of bead-bound cells under the influence of flow rates ranging from 1 to 5 mL min^{-1}. Fig. 4(b) shows the effect of flow rate on discriminating cells based on the number of beads they are bound to. According to Fig. 4(b), the optimal flow rate of our system is about 2 mL min^{-1} since at this flow rate, cells bound with 7 or more beads (90% of cancer cells) encounter the chip surface with a probability of 96% or greater. At the same time, cells that are bound to fewer than 4 beads (90% of bead-bound WBCs) encounter the chip surface with a much lower probability. This relatively simple computational

model only accounts for a cell's motion until it encounters the chip surface and not what happens afterwards (e.g. bouncing off, colliding with other particles, or moving on the chip surface etc.). However it effectively confirms the basic interplay between the flow rate and the number of beads and suggests that an optimal choice of a flow rate could help reduce capturing unintended cells that are bound to small number of beads non-specifically without significantly hampering the specific capturing of cancer cells, and that too low a flow rate (e.g. < 2 mL min^{-1}) could increase the capture of unintended cells without a significant improvement in the detection of specific cancer cells. In fact, when flow rate is lower than 1 mL min^{-1}, magnetic forces greatly outweigh fluidic forces which causes the beads to pile up and hide rare target cells underneath (see Fig. S2 in the ESI†).

To verify the relationship between the capture yield of cancer cells and the detection flow rate suggested by the simulations, MCF-7 cells were first incubated with anti-EpCAM beads in PBS buffer using the protocols described previously. We then spiked 70 MCF-7 cells pre-labeled with anti-EpCAM
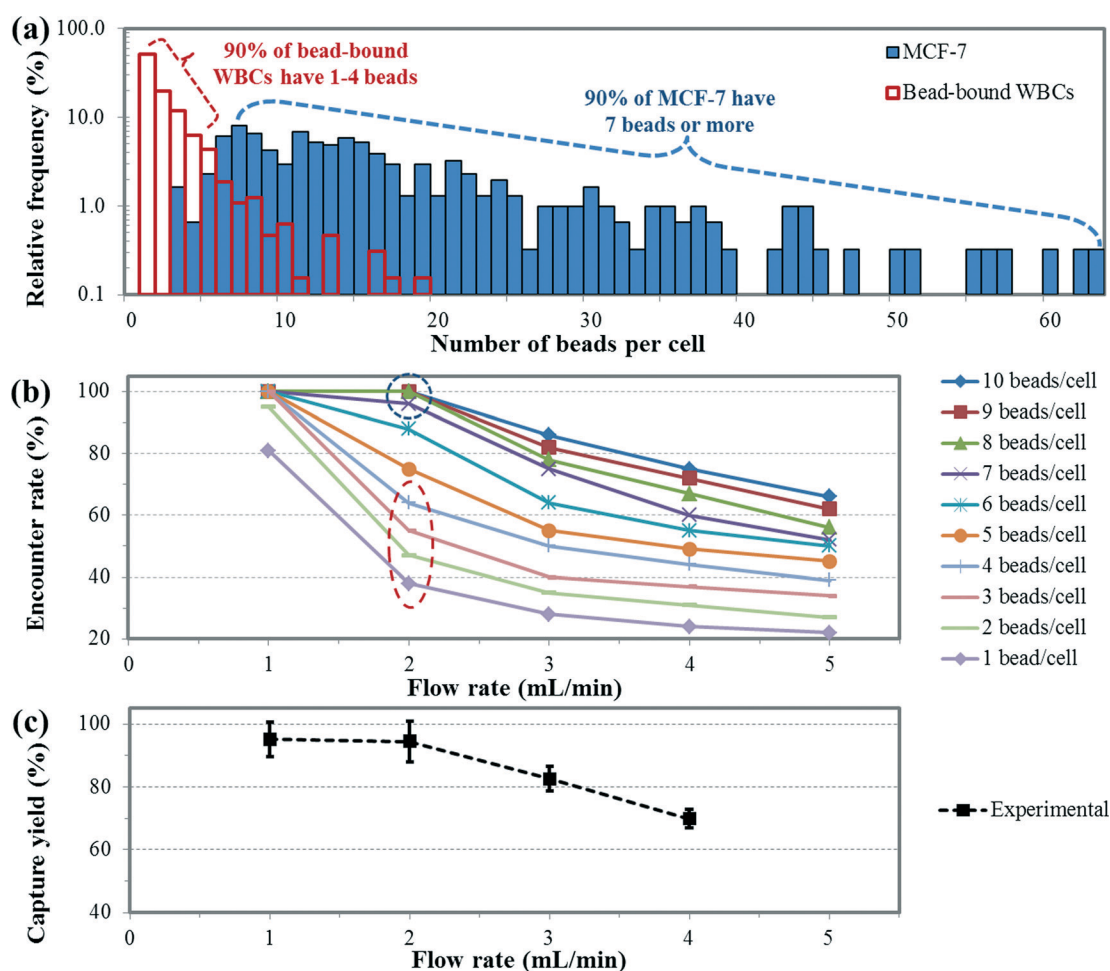

Fig. 4 (a) Histograms in semi log-scale showing distribution of number of anti-EpCAM beads bound on MCF-7 cells and white blood cells (WBCs). All MCF-7 cells bound to at least 3 beads, while over 99% of WBCs did not bind to any beads. The relative frequency was calculated only for cells that bound to beads. (b) Simulated chip surface encounter rate of 100 cell–beads complexes vs. the flow rate. (c) Capture yield of pre-labeled MCF-7 cells (with beads) spiked in blood vs. the flow rate. Error bars indicate standard deviations from 3 measurements.

beads into 1 mL of blood, following by removal of RBCs using lysis buffer. The remaining cells were re-suspended in 1.5 mL of PBS buffer and run through the fluidic chamber at flow rates ranging from 1 to 4 mL min^{-1} (our pump's max flow rate does not reach 5 mL min^{-1}). The number of MCF-7 cells captured on the microchip was enumerated under a microscope and the capture rates were plotted against flow rate in Fig. 4(c). In this plot the capture yield is around 95% at both 1 and 2 mL min^{-1}, and starts to decrease with increasing flow rate. Despite a negative 5% offset in the capture yield that is presumably due to imperfections in affinity or centrifugation after the RBC lysing step, the experimental result in Fig. 4(c) is in good agreement with the simulated data in Fig. 4(b) and confirms the optimal flow rate suggested by the simulations.

Due to the relatively large cross sectional dimensions of the chamber (3.8 mm by 2 mm) and hence the relatively low velocities (~4.4 mm s^{-1} for 2 mL min^{-1}), the resulting shear rates are low in comparison with those that occur in the human blood circulation and hence do not cause damage to the cells on the chip surface (see ESI†).

Dual magnet model

The primary magnetic force that attracts the bead-bound cells to the chip surface is generated by the magnet situated below the fluidic chamber. However, this arrangement may result in a number of free beads that land between the apertures and therefore remain on the chip. A simple modification to the setup clears these free beads out by perturbing the total magnetic field with a second magnet (whose polarity is aligned for attraction to the primary magnet) situated on top of the chamber. Manually moving this magnet horizontally in an oscillatory fashion perturbs the horizontal magnetic force on the beads and hence leads them into an aperture. We developed a computational model of this effect in order to quantify it. The analysis was performed under the assumption of zero flow rate since it focuses on the beads that have already been captured on the chip surface. Fig. 5(a) shows the magnetic flux density distribution in the chamber when the top magnet (3/16" × 3/16" × 3/16") is aligned with the center of the bottom magnet (1/4" × 1/4" × 1/4"), as well as when it is located to the left to the bottom magnet. The corresponding magnetic forces applied on a bead with respect to its position on the chip are shown in Fig. 5(b). The simulation result shows that the horizontal motion of the top magnet causes significant changes in the magnetic flux density distribution, which alters the magnetic force induced on the beads in the chamber, especially in the horizontal direction. As a result, the free beads located in between the apertures on the chip move horizontally along with the motion of the top magnet. We simulated the horizontal motion of a bead located on the surface of the central region of the chip and observed that a 3 mm sideways motion of the top magnet caused the bead to move by 150 μm which is sufficient to lead it to an aperture to be pulled down by the vertical

magnetic force. Fig. 5(c) demonstrates the simulated motion of a bead located at the center of the microchip. The bead reached an adjacent aperture and fell through it with only a 200 μm motion of the top magnet. Therefore, moving the top magnet by as many as a few millimetres should effectively clear out most of the free beads that do not initially coincide with an aperture (Fig. 5(d) and (e)). It is also plausible that the dual magnet configuration can help clear out the unwanted bead-bound blood cells that are smaller than 8 μm and hence result in higher purity.

(2) System characterization

We next investigated the system's ability to recognize and capture tumor cells spiked into blood samples of healthy humans. We spiked known number (0, 8, 10, 20, 30, 40, 50, 60, 70, 100, and 110) of MCF-7 cells into 8 mL of blood, and captured them using anti-EpCAM beads. Based on the computational study and the experiments discussed above, ideally around 95% of the spiked tumor cells could encounter the chip surface when the sample mixture flows through the chamber at 2 mL min^{-1}. However, the actual detection yield is expected to be lower because of a number of factors. For example some cells could be lost during centrifugation after RBC lysing step or during incubation with beads, also the binding efficiency between MCF-7 cells and antibody-beads could be impeded due to the complexity of the binding environment. It is therefore important to minimize additional losses once the bead-bound cells are introduced into the chamber. The high flow rate capability of our system allows us to quickly circulate the sample mixture multiple times and help maximize the chances of recovering a cell that may have skipped the chip surface during its first pass. We therefore circulated the sample at 2 mL min^{-1} for 3 minutes, equivalent to passing it through the chamber 4 times over.

Immunofluorescence analysis of the cells captured on the microchip was performed while they were still on the chip within the chamber. Fig. 6(a) shows bright-field and fluorescent images of an area on a microchip that contains some captured cells. The anti-CK-FITC bound to MCF-7 cells emitted green fluorescent light, while the anti-CD45-PE bound to the white blood cells (WBCs) emitted red light. DAPI stained the cell nuclei and emitted blue light. We identified tumor cells based on a combination of factors including the size (10–30 μm) and shape (close to circular) of the cells, and the fluorescent emissions (CK+, DAPI+ and CD45-). The cells that did not fit this description may have nonspecifically bound to either the beads and/or the chip surface and were not scored as a tumor cell. Enumeration of the detected tumor cells was performed manually by capturing images of different segments of the chip surface and counting the cells in each segment. A plot of the number of cells detected vs. number of those spiked is shown in Fig. 6(b). The slope of the linear fit shows that the system can detect cells with an 89% detection yield and the fairly linear nature of the relationship
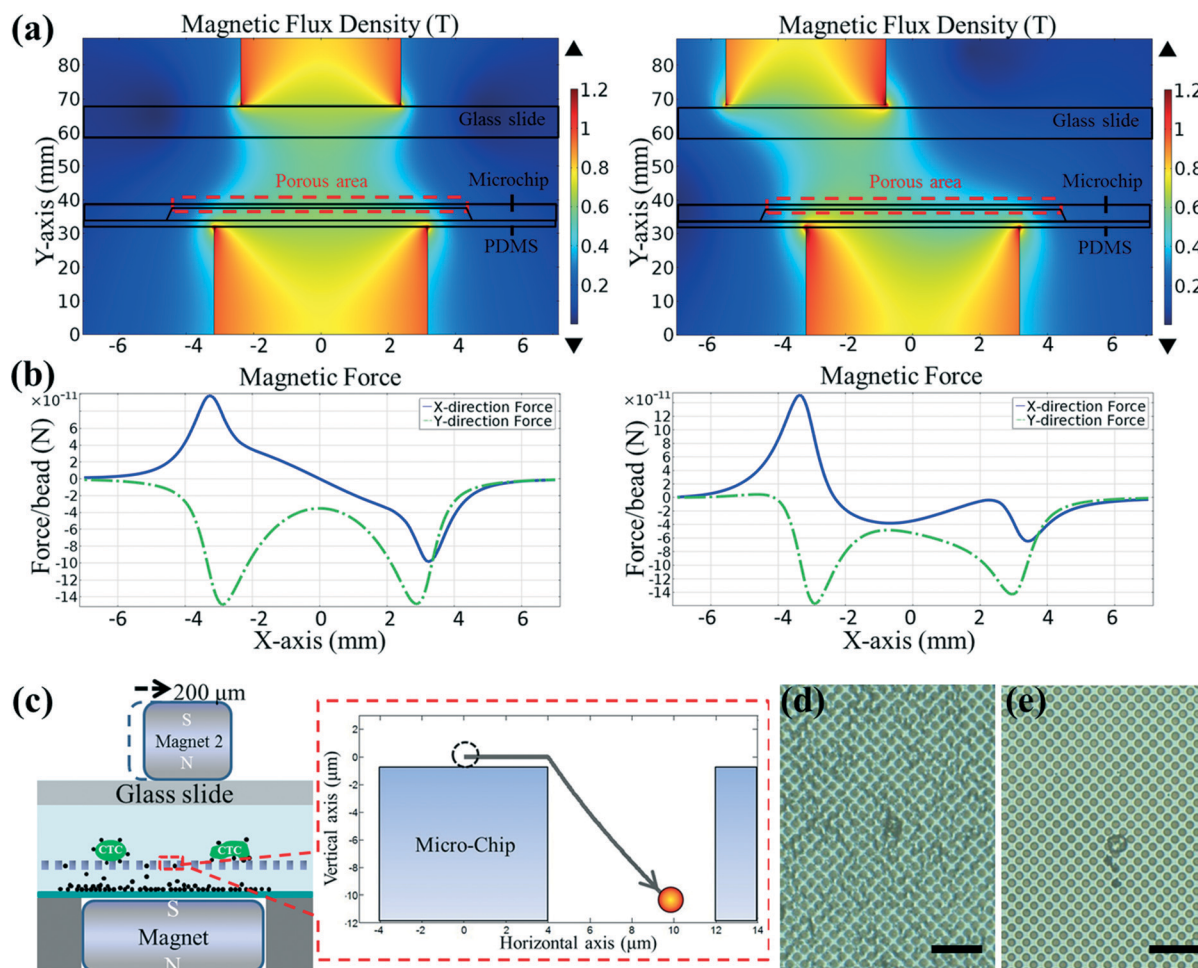
Fig. 5 (a) The simulated magnetic flux density of the dual magnet configuration and (b) the corresponding magnetic force applied on a single bead in the fluidic chamber. (c) Schematic illustrating the motion of a bead located at the center of the micro-chip with respective to the movement of the top magnet. The 10 μm lateral displacement of the bead results from the 200 μm lateral movement of the top magnet. The schematic was not drawn to scale. (d) (e) Micrographs of chip surfaces without and with the use of a second magnet after capture to clear out the free beads. Scale bars indicate 56 μm.

shows that the system robustly delivers this efficiency at a wide range of cell concentrations.

(3) Detection of CTCs from cancer patient samples

We next detected CTCs in the blood samples obtained from patients with advanced cancer. Blood samples collected from a total of 50 patients with NSCLC ($n = 38$) and PANC ($n = 12$) were tested using our system. All of the patients had stage IV metastatic diseases and 20 of the NSCLC patients and 5 of the PANC patients had not received systemic treatment. 4 to 8 mL blood from each patient was examined following the same protocol used in detection of MCF-7 cells spiked in blood except for the choice of the antibody-beads. Unlike the cancer cell lines that are always cultured in a simple and controlled laboratory environment, the CTCs from patients may vary in their expression and affinity for the EpCAM antibody. As discussed before, we used a combination of beads conjugated with different antibodies to target multiple antigens overexpressed on CTCs. A combination of beads conjugated with anti-EpCAM, anti-EGFR and anti-VMT at a ratio of $1:1:1$ was used to test NSCLC samples; while a combination of anti-EpCAM and anti-CEA beads ($1:1$) were used for PANC samples. The anti-EGFR and anti-CEA were used to target an extra antigen (other than EpCAM) that could possibly be overexpressed on CTCs in lung and pancreatic cancers, respectively. On the other hand, anti-VMT beads were used to target any CTCs that may be going through epithelial-to-mesenchymal transition.

The fluorescent images of the cells detected from NSCLC and PANC samples are displayed in Fig. 7(a) and (b), respectively. Once again only those cells showing CK+, DAPI+ and meanwhile CD45- were identified as CTCs. Notice that in Fig. 7(a) the cell in the middle only shows DAPI+ but is stained by neither CK nor CD45. This could be a blood cell present in the sample that does not express either of CK or CD45, or a tumor cell that has gone through EMT and lost its epithelial markers. Nevertheless, these rare cells were not
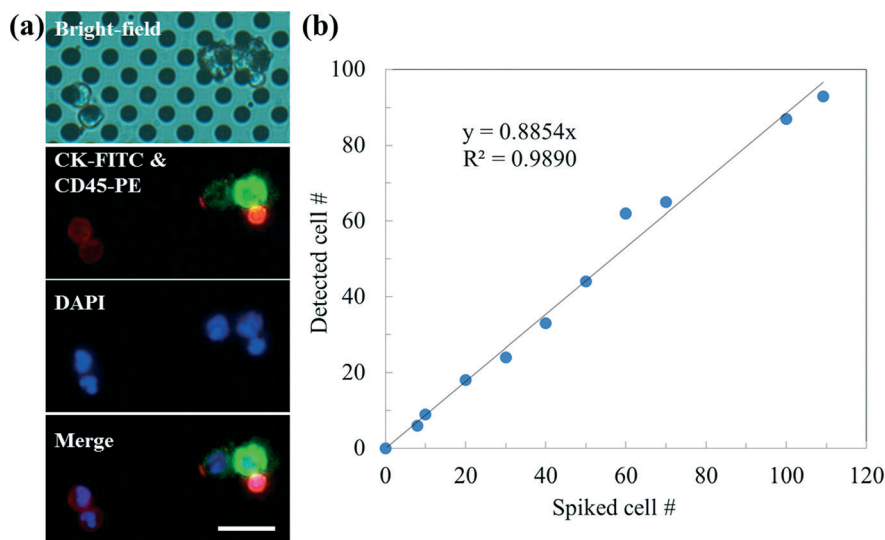
Fig. 6 (a) Bright-field and fluorescent images of cells detected from MCF-7-spiked blood. MCF-7 cells are stained with CK-FITC and thus show green fluorescence; while WBCs are stained with CD45-PE and show red. Scale bar indicates 24 μm. The contrast of the fluorescent images has been enhanced artificially. (b) Number of MCF-7 cells detected vs. number of those spiked in blood.
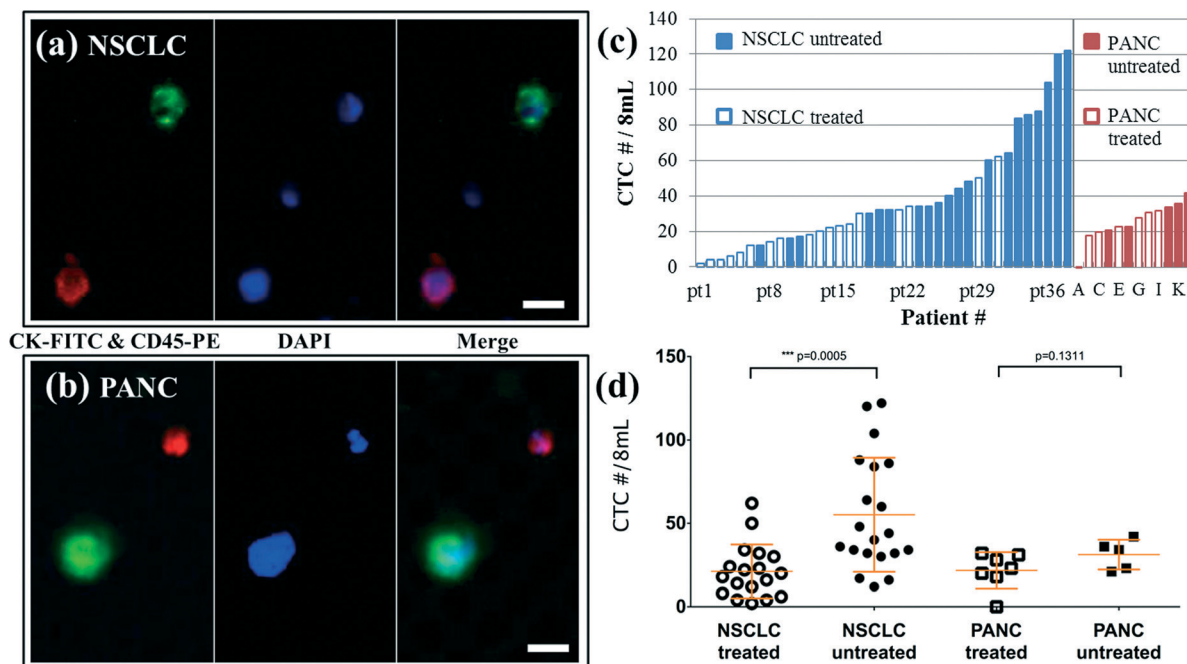

Fig. 7 (a) Fluorescent images of cells detected from (a) NSCLC and (b) PANC patients. Cells show both green and blue in merged images are CK+, DAPI+ and CD45-, and hence are identified as CTCs. Scale bars indicate 12 μm. The contrast of the fluorescent images has been enhanced artificially. (c) Histograms showing number of CTCs detected from each of the 50 patients. (d) The mean, standard deviation and p-value of number of CTCs detected from treated and untreated patients.

included in the CTC count. We also observed some triple-positive cells (both CK+ and CD45+, with DAPI+) that also were excluded from the CTC count.

The number of CTCs per 8 mL of blood of each patient is shown in Fig. 7(c). We identified CTCs in 49 of 50 patients. Only one PANC patient that had received chemotherapy recently did not show any CTCs. The number of CTCs detected ranged from 2 to 122 per 8 mL for NSCLC and 0 to 42 per

8 mL for PANC, resulting in a mean and standard deviation of 39 ± 32 CTCs/8 mL for NSCLC and 26 ± 11 CTCs/8 mL for PANC. The purity of the detection was also analyzed by calculating the log depletion of WBCs which are the major source of impurities. For NSCLC samples, the number of DAPI positive cells found on chips ranged from 868 to 19 916 with an average of 4016 (from 8 mL of blood), which yields an average of 4-log depletion of WBCs. On the other

hand, our system achieved an average of 3.6-log depletion of WBCs while detecting CTCs from PANC blood samples.

We further grouped the number of CTCs detected from patients who had received systemic cancer treatments as well as from those who had not and plotted them in Fig. 7(d). On average we detected 55 CTCs in the blood samples of untreated NSCLC patients and 21 in those of treated ones; meanwhile, the average CTC counts of the untreated and treated PANC patients are 31 and 22. A student t-test analysis on the two groups of NSCLC patients revealed a p-value of 0.00045, indicating a statistically significant difference between the CTC counts of the two groups. On the other hand, presumably due to relatively smaller sample size, the p-value of the average count between the treated and untreated PANC data is 0.13114 indicating that the difference is statistically insignificant. Our current efforts are focused on comparing CTCs isolated from the same patient before and after systemic treatment to assess our system's capability to detect CTC response to treatment.

Conclusions

We have demonstrated a microchip system that combines immunomagnetics, high-flow rate fluidics and size-based separation, for detection of CTCs. Cells captured can be imaged and enumerated directly on the microchip. The optimal flow rate for CTC detection was found to be 2 mL min^{-1} based on a computational model that was also verified experimentally. With the optimized flow rate, 89% of the MCF-7 cells spiked in 8 mL of blood were detected. We further applied the system to the analysis of clinical samples obtained from NSCLC and PANC patients using cocktails of antibody-beads and have detected CTCs in all 38 NSCLC patients and 11 of 12 PANC patients. Moreover, the data demonstrated a statistically significant difference in the number of CTCs between treated and untreated NSCLC patients, which warrants further analyses and studying of the correlation between the CTCs detected by this system and the overall tumor burden. Due to its versatility, robustness, relative architectural simplicity, and compatibility with existing practices, we envision this system to be highly beneficial in clinical and research settings.

Acknowledgements

References

1 P. Mehlen and A. Puisieux, *Nat. Rev. Cancer*, 2006, **6**, 449–458.

2 S. Mocellin, D. Hoon, A. Ambrosi, D. Nitti and C. R. Rossi, *Clin. Cancer Res.*, 2006, **12**, 4605–4613.

3 K. Pantel and C. Alix-Panabieres, *Trends Mol. Med.*, 2010, **16**, 398–406.

4 N. Aceto, A. Bardia, D. T. Miyamoto, M. C. Donaldson, B. S. Wittner, J. A. Spencer, M. Yu, A. Pely, A. Engstrom, H. Zhu, B. W. Brannigan, R. Kapur, S. L. Stott, T. Shioda, S. Ramaswamy, D. T. Ting, C. P. Lin, M. Toner, D. A. Haber and S. Maheswaran, *Cell*, 2014, **158**, 1110–1122.

5 C. L. Hodgkinson, C. J. Morrow, Y. Li, R. L. Metcalf, D. G. Rothwell, F. Trapani, R. Polanski, D. J. Burt, K. L. Simpson, K. Morris, S. D. Pepper, D. Nonaka, A. Greystoke, P. Kelly, B. Bola, M. G. Krebs, J. Antonello, M. Ayub, S. Faulkner, L. Priest, L. Carter, C. Tate, C. J. Miller, F. Blackhall, G. Brady and C. Dive, *Nat. Med.*, 2014, **20**, 897–903.

6 A. A. Adams, P. I. Okagbare, J. Feng, M. L. Hupert, D. Patterson, J. Gottert, R. L. McCarley, D. Nikitopoulos, M. C. Murphy and S. A. Soper, *J. Am. Chem. Soc.*, 2008, **130**, 8633–8641.

7 R. A. Nagourney, *Curr. Treat. Options Oncol.*, 2006, **7**, 103–110.

8 S. Nagrath, L. V. Sequist, S. Maheswaran, D. W. Bell, D. Irimia, L. Ulkus, M. R. Smith, E. L. Kwak, S. Digumarthy, A. Muzikansky, P. Ryan, U. J. Balis, R. G. Tompkins, D. A. Haber and M. Toner, *Nature*, 2007, **450**, 1235–1239.

9 S. L. Stott, C. H. Hsu, D. I. Tsukrov, M. Yu, D. T. Miyamoto, B. A. Waltman, S. M. Rothenberg, A. M. Shah, M. E. Smas, G. K. Korir, F. P. Floyd Jr., A. J. Gilman, J. B. Lord, D. Winokur, S. Springer, D. Irimia, S. Nagrath, L. V. Sequist, R. J. Lee, K. J. Isselbacher, S. Maheswaran, D. A. Haber and M. Toner, *Proc. Natl. Acad. Sci. U. S. A.*, 2010, **107**, 18392–18397.

10 M. Gerlinger, A. J. Rowan, S. Horswell, J. Larkin, D. Endesfelder, E. Gronroos, P. Martinez, N. Matthews, A. Stewart, P. Tarpey, I. Varela, B. Phillimore, S. Begum, N. Q. McDonald, A. Butler, D. Jones, K. Raine, C. Latimer, C. R. Santos, M. Nohadani, A. C. Eklund, B. Spencer-Dene, G. Clark, L. Pickering, G. Stamp, M. Gore, Z. Szallasi, J. Downward, P. A. Futreal and C. Swanton, *N. Engl. J. Med.*, 2012, **366**, 883–892.

11 J. M. Wu, M. J. Fackler, M. K. Halushka, D. W. Molavi, M. E. Taylor, W. W. Teo, C. Griffin, J. Fetting, N. E. Davidson, A. M. De Marzo, J. L. Hicks, D. Chitale, M. Ladanyi, S. Sukumar and P. Argani, *Clin. Cancer Res.*, 2008, **14**, 1938–1946.

12 D. Weinstat-Saslow and P. S. Steeg, *FASEB J.*, 1994, **8**, 401–407.

13 F. A. Coumans, S. T. Ligthart, J. W. Uhr and L. W. Terstappen, *Clin. Cancer Res.*, 2012, **18**, 5711–5718.

14 S. H. Cho, J. M. Godin, C. H. Chen, W. Qiao, H. Lee and Y. H. Lo, *Biomicrofluidics*, 2010, **4**, 043001.

15 S. Riethdorf, H. Fritsche, V. Muller, T. Rau, C. Schindlbeck, B. Rack, W. Janni, C. Coith, K. Beck, F. Janicke, S. Jackson, T. Gornet, M. Cristofanilli and K. Pantel, *Clin. Cancer Res.*, 2007, **13**, 920–928.

16 M. Cristofanilli, D. F. Hayes, G. T. Budd, M. J. Ellis, A. Stopeck, J. M. Reuben, G. V. Doyle, J. Matera, W. J. Allard, M. C. Miller, H. A. Fritsche, G. N. Hortobagyi and L. W. Terstappen, *J. Clin. Oncol.*, 2005, **23**, 1420–1430.

17 S. K. Arya, B. Lim and A. R. Rahman, *Lab Chip*, 2013, **13**, 1995–2027.

18 P. Li, Z. S. Stratton, M. Dao, J. Ritz and T. J. Huang, *Lab Chip*, 2013, **13**, 602–609.

19 P. Chen, Y. Y. Huang, K. Hoshino and X. Zhang, *Lab Chip*, 2014, **14**, 446–458.

20 M. E. Warkiani, G. Guan, K. B. Luan, W. C. Lee, A. A. Bhagat, P. K. Chaudhuri, D. S. Tan, W. T. Lim, S. C. Lee, P. C. Chen, C. T. Lim and J. Han, *Lab Chip*, 2014, **14**, 128–137.

21 E. Ozkumur, A. M. Shah, J. C. Ciciliano, B. L. Emmink, D. T. Miyamoto, E. Brachtel, M. Yu, P. I. Chen, B. Morgan, J. Trautwein, A. Kimura, S. Sengupta, S. L. Stott, N. M. Karabacak, T. A. Barber, J. R. Walsh, K. Smith, P. S. Spuhler, J. P. Sullivan, R. J. Lee, D. T. Ting, X. Luo, A. T. Shaw, A. Bardia, L. V. Sequist, D. N. Louis, S. Maheswaran, R. Kapur, D. A. Haber and M. Toner, *Sci. Transl. Med.*, 2013, **5**, 179ra147.

22 N. M. Karabacak, P. S. Spuhler, F. Fachin, E. J. Lim, V. Pai, E. Ozkumur, J. M. Martel, N. Kojic, K. Smith, P. I. Chen, J. Yang, H. Hwang, B. Morgan, J. Trautwein, T. A. Barber, S. L. Stott, S. Maheswaran, R. Kapur, D. A. Haber and M. Toner, *Nat. Protoc.*, 2014, **9**, 694–710.

23 W. Sheng, T. Chen, R. Kamath, X. Xiong, W. Tan and Z. H. Fan, *Anal. Chem.*, 2012, **84**, 4199–4206.

24 W. Sheng, T. Chen, W. Tan and Z. H. Fan, *ACS Nano*, 2013, **7**, 7067–7076.

25 K. Hoshino, Y. Y. Huang, N. Lane, M. Huebschman, J. W. Uhr, E. P. Frenkel and X. Zhang, *Lab Chip*, 2011, **11**, 3449–3457.

26 C. M. Earhart, C. E. Hughes, R. S. Gaster, C. C. Ooi, R. J. Wilson, L. Y. Zhou, E. W. Humke, L. Xu, D. J. Wong, S. B. Willingham, E. J. Schwartz, I. L. Weissman, S. S. Jeffrey, J. W. Neal, R. Rohatgi, H. A. Wakelee and S. X. Wang, *Lab Chip*, 2014, **14**, 78–88.

27 M. Hosokawa, T. Hayata, Y. Fukuda, A. Arakaki, T. Yoshino, T. Tanaka and T. Matsunaga, *Anal. Chem.*, 2010, **82**, 6629–6635.

28 S. Zheng, H. Lin, J. Q. Liu, M. Balic, R. Datar, R. J. Cote and Y. C. Tai, *J. Chromatogr. A*, 2007, **1162**, 154–161.

29 S. Zheng, H. K. Lin, B. Lu, A. Williams, R. Datar, R. J. Cote and Y. C. Tai, *Biomed. Microdevices*, 2011, **13**, 203–213.

30 M. Alunni-Fabbroni and M. T. Sandri, *Methods*, 2010, **50**, 289–297.

31 L. S. Lim, M. Hu, M. C. Huang, W. C. Cheong, A. T. Gan, X. L. Looi, S. M. Leong, E. S. Koay and M. H. Li, *Lab Chip*, 2012, **12**, 4388–4396.

32 A. Lee, J. Park, M. Lim, V. Sunkara, S. Y. Kim, G. H. Kim, M. H. Kim and Y. K. Cho, *Anal. Chem.*, 2014, **86**, 11349–11356.

33 E. Sollier, D. E. Go, J. Che, D. R. Gossett, S. O'Byrne, W. M. Weaver, N. Kummer, M. Rettig, J. Goldman, N. Nickols, S. McCloskey, R. P. Kulkarni and D. Di Carlo, *Lab Chip*, 2014, **14**, 63–77.

34 C. Chang, S. Jalal, W. Huang, A. Mahmood, D. Matei and C. Savran, *IEEE Sens. J.*, 2014, **14**, 3008–3013.

35 A. Memic, A. Hasan, M. Akbari, M. R. Dokmeci and A. Khademhosseini, *Lab Chip*, 2013, **13**, 4157.

36 G. Selvaggi, S. Novello, V. Torri, E. Leonardo, P. De Giuli, P. Borasio, C. Mossetti, F. Ardissone, P. Lausi and G. V. Scagliotti, *Ann. Oncol.*, 2004, **15**, 28–32.

37 P. Cen, X. Ni, J. Yang, D. Y. Graham and M. Li, *Biochim. Biophys. Acta*, 1826, **2012**, 350–356.

38 S. A. Mani, W. Guo, M. J. Liao, E. N. Eaton, A. Ayyanan, A. Y. Zhou, M. Brooks, F. Reinhard, C. C. Zhang, M. Shipitsin, L. L. Campbell, K. Polyak, C. Brisken, J. Yang and R. A. Weinberg, *Cell*, 2008, **133**, 704–715.

39 A. D. Rhim, E. T. Mirek, N. M. Aiello, A. Maitra, J. M. Bailey, F. McAllister, M. Reichert, G. L. Beatty, A. K. Rustgi, R. H. Vonderheide, S. D. Leach and B. Z. Stanger, *Cell*, 2012, **148**, 349–361.

40 A. J. Armstrong, M. S. Marengo, S. Oltean, G. Kemeny, R. L. Bitting, J. D. Turnbull, C. I. Herold, P. K. Marcom, D. J. George and M. A. Garcia-Blanco, *Mol. Cancer Res.*, 2011, **9**, 997–1007.

41 N. F. Steinmetz, C. F. Cho, A. Ablack, J. D. Lewis and M. Manchester, *Nanomedicine*, 2011, **6**, 351–364.

42 U. H. Weidle, D. Maisel, S. Klostermann, C. Schiller and E. H. Weiss, *Cancer Genomics Proteomics*, 2011, **8**, 49–63.

43 A. Satelli, A. Mitra, J. J. Cutrera, M. Devarie, X. Xia, D. R. Ingram, D. Dibra, N. Somaiah, K. E. Torres, V. Ravi, J. A. Ludwig, E. S. Kleinerman and S. Li, *Cancer Res.*, 2014, **74**, 1645–1650.

44 S. S. Shevkoplyas, A. C. Siegel, R. M. Westervelt, M. G. Prentiss and G. M. Whitesides, *Lab Chip*, 2007, **7**, 1294–1302.

45 E. P. Furlani and K. C. Ng, *Phys. Rev. E: Stat., Nonlinear, Soft Matter Phys.*, 2008, 77, 061914.

46 B. D. Chan, K. Icoz, W. Huang, C. L. Chang and C. A. Savran, *Lab Chip*, 2014, **14**, 4188–4196.